Vol. **113** (2008) *ACTA PHYSICA POLONICA A* No. 2

Studies of the Hydrodynamic Properties of Bose–Einstein Condensate of ^{87}Rb Atoms in a Magnetic Trap

F. Bylicki[a,b], W. Gawlik[a,c], W. Jastrzębski[a,d], A. Noga[a,c], J. Szczepkowski[a,e], M. Witkowski[a,f], J. Zachorowski[a,c] and M. Zawada[a,b,*]

[a]National Laboratory for Atomic Molecular and Optical Physics
Grudziądzka 5, 87-100 Toruń, Poland,
[b]Institute of Physics, Nicolaus Copernicus University
Grudziądzka 5, 87-100 Toruń, Poland
[c]Institute of Physics, Jagiellonian University
Reymonta 4, 30-057 Kraków, Poland
[d]Institute of Physics, Polish Academy of Sciences
al. Lotników 32-46, 02-668 Warszawa, Poland
[e]Institute of Physics, Pomeranian Academy
Arciszewskiego 22b, 76-200, Słupsk, Poland
[f]Institute of Physics, University of Opole
Oleska 48, 45-052 Opole, Poland

(Received November 27, 2007; revised version December 21, 2007)

We report details of the apparatus and the experimental procedure leading to production of the Bose–Einstein condensate of ^{87}Rb atoms. Basic hydrodynamic properties of the condensate, like quadrupole oscillations and free fall expansion, are investigated. They provide also characteristics of the magnetic trap crucial for interpretation of future experiments.

PACS numbers: 03.75.Hh, 03.75.Kk, 67.85.Bc, 67.85.De

1. Introduction

We report on our experiments aiming at realization of a Bose–Einstein condensate (BEC) of ^{87}Rb atoms in a magnetic trap and determination of its main hydrodynamic properties. The Bose–Einstein condensation is a form of quantum

*corresponding author; e-mail: zawada@fizyka.umk.pl

degeneracy which occurs when the phase-space density in the investigated system reaches unity. This requires substantial increase in the atomic de Broglie wavelength by reducing atomic velocities, i.e. cooling, and reducing their mean distances, i.e. compression, while avoiding strong atom–atom interaction. Typical approach to reach this objective is employment of the laser cooling together with magneto-optical and magnetic trapping techniques. In our work we use a special form of a magnetic trap, developed by the Dalibard team [1], which can be realized with relatively low electric currents. The setup allows generation of pure BEC of about 100 000 atoms at a temperature lower then 70 nK.

The basic properties of BEC and their various experimental realizations have been extensively described in literature [2-4], so in this paper we concentrate on the specific details of our apparatus (Sect. 2), description of our experiment (Sect. 3), and results of our measurements of the hydrodynamic properties of BEC (Sect. 4), which are summarized and concluded in Sect. 5.

2. Apparatus

2.1. Vacuum system

The vacuum system (Fig. 1) is composed of two chambers, the upper and the lower one, which are connected by a thin stainless steel tube. Such construction is necessary for obtaining different pressure conditions for the preparatory and condensation stages of the experiment. Both chambers are independently pumped (differential pumping) with ion pumps of 25 l/s speed (upper) and 55 l/s (lower chamber). The lower section is also connected with a titanium sublimation pump.

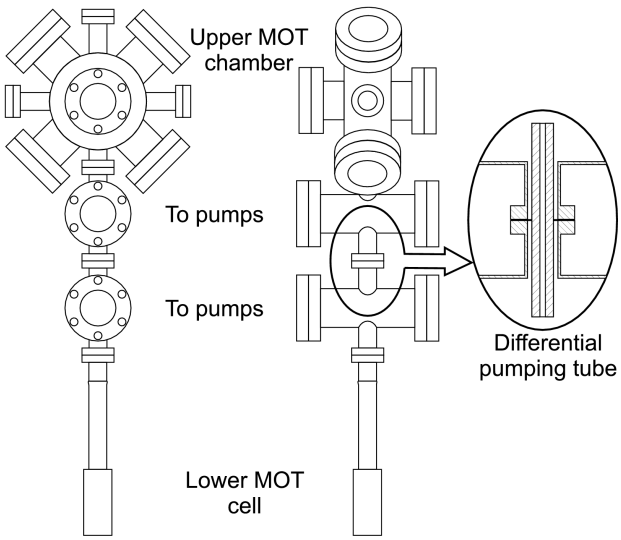

Fig. 1. Schematic drawing of the vacuum system. The positions of the upper and lower MOTs are indicated. The magnetic trap center coincides with the lower MOT position. The position of the graphite tube providing the differential pumping is shown in the inset.

Additionally, it was found that a graphite tube (120 mm long and with 4.5 mm internal diameter) placed inside the steel tube improved ultra high vacuum in the lower chamber and allowed to maintain stable pressure difference of three orders of magnitude between the two chambers. The upper chamber is made of stainless steel with pyrex windows antireflection coated for 780 nm and houses the magneto-optical trap (upper MOT) which collects ^{87}Rb atoms from the thermal vapor. The chamber is loaded from a rubidium metal dispenser (SAES Getters) [5]. Typically, the Rb vapor pressure in the upper chamber is 1×10^{-8} mbar which is crucial for obtaining a sufficiently high number of atoms in the upper MOT and adequately high flux of cold atoms transferred to the lower chamber across the graphite tube. The lower chamber is a quartz cuvette where atoms are loaded to the lower MOT and magnetic trap. Typical pressure in the lower chamber is 1×10^{-11} mbar.

2.2. Upper MOT

The upper magneto-optical trap is created by three orthogonal, retro--reflected pairs of laser beams of circular polarization. The trapping laser is red detuned by two natural widths Γ, $\Gamma = 6$ MHz, from the cooling transition $5^2S_{1/2}\ |F = 2\rangle \rightarrow 5^2P_{3/2}\ |F = 3\rangle$ of the ^{87}Rb D_2 line. The diameter of the beams is 17 mm, the power in each one is 40 mW. The repumping beam of 25 mW power and 17 mm diameter is added to one of the trapping beams. The quadrupole magnetic field of 12 G/cm axial gradient is created by a pair of coils in the anti-Helmholtz configuration. When the Rb dispenser is heated with 3.8 A current the trap is loaded to some 10^8 atoms in 5 s. The temperature of atoms in the upper MOT is typically about 500 μK.

2.3. Transfer of atoms

A vertical, CW transfer laser beam acts on atoms in the upper MOT and pushes them downwards, towards the lower vacuum chamber, where the second MOT is created (Fig. 1). The distance between the two traps is 415 mm. We have experimentally established that the best transfer efficiency is reached when the circularly polarized transfer beam of 4 mW is detuned 2Γ below the atomic resonance. To minimize the effect of the transfer beam on the lower MOT, a lens system was used to spatially shape the beam so that it was focused to the waist of 50 μm radius at the point 0.5 cm above the upper MOT and diverged to above 3 mm radius at the lower MOT. Since the transfer beam is not mixed with the repumper beam, as soon as the atoms leave the upper MOT they are optically pumped to the dark hyperfine state ($F_{\mathrm{g}} = 1$) and are neither further accelerated nor additionally heated. In our system, the most efficient transfer is obtained when the transfer beam is directed not through the MOT cloud center but rather through its edge.

2.4. Lower MOT

The lower magneto-optical trap is formed in the quartz cuvette at the crossing point of six independent beams of 10 mm diameter and 40 mW power each.

Similarly as in the upper MOT, the frequency of the trapping laser is kept at 2Γ below the atomic $F_g = 2 - F_e = 3$ transition but, unlike in the upper trap, in the lower MOT the repumping beam (10 mm diameter, power 80 mW) is mixed with the trapping beam before splitting into the six independent beams. Such a configuration has been chosen to avoid imbalance of the optical forces caused by light absorption in a dense sample and warrants regular and stable shape of the atomic cloud, important for efficient loading of the magnetic trap. Two coils produce the quadrupole magnetic field of 10 G/cm axial gradient. After 20 s of transferring cold atoms from the upper MOT the trap gathers some 10^9 atoms of about 500 μK temperature and density 1×10^{11} cm^{-3}.

2.5. Magnetic trap

The setup of the magnetic trap (MT) is dictated by the compromise between the requirements of broad optical access to the quartz cuvette and the effort to minimize the coil currents and the related problems with fast switching. The construction is based on the setup presented in [1]. The trap magnetic field is produced by three identical conical coils and two large coils producing the offset field (Fig. 2). They form the Joffe–Pritchard-type field configuration with $B_{\min} > 0$ to avoid the trap losses due to the Majorana spin-flips [6]. The setup is

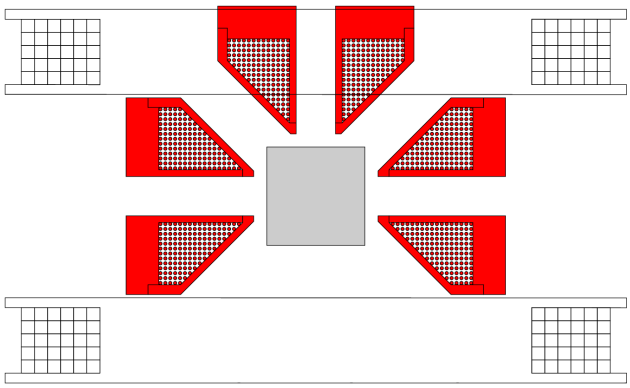

Fig. 2. Horizontal cross-section of the windings in the magnetic trap. Three conical coils and two offset coils are shown. Additional coils for the MOT field and compensation are not shown.

similar to the quadrupole Ioffe–Pritchard configuration (QUIC) [7], but in the original QUIC the position of the potential minimum shifts significantly in the process of adiabatic compression which occurs during the passage from the quadrupole to the Ioffe-Pritchard conditions. While the configuration of three identical coils requires an extra pair of coils to lower the $B_{\min}$ field (the offset coils) and to compress the cloud of atoms, it has the advantage of creating the potential minimum in the same position as two quadrupole coils. Conical shaping of the MT coils allows placing them close to the cuvette with relatively small obstruction of the

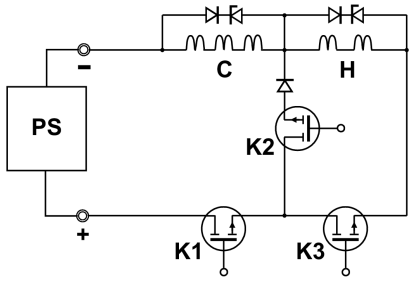

Fig. 3. Schematic of the electronic circuit for controlling currents in the conical (C) and offset (H) coils of the magnetic trap. PS is the power supply, keys K1, K2, and K3 are MOSFETs (IRF260N). The diode sets connected in parallel with the coils consist of regular diodes (D42-12 N0) and high-voltage Zener diodes (1.5 KE91 A). The diode in series with K2 is a regular high power diode.

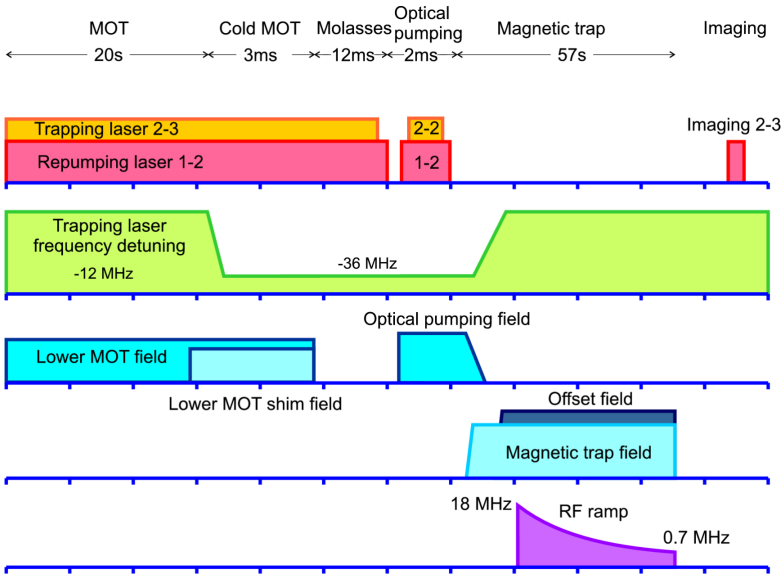

Fig. 4. Timing of the experiment. The upper MOT and the transfer beam are functioning for the first 20 s. Two top lines refer to laser fields, two next lines to the magnetic field, and the bottom line to the RF evaporation field.

optical access and their close separation lowers the currents to a convenient level of 40–50 A. Each conical coil has 161 windings of copper wire of 1 mm diameter and is cooled by water flowing between individual wires within the conical enclosure. This design [1] allows efficient absorption of 500 W power dissipated by each coil. The offset coils have 2×31 windings of a copper tubing of 3 mm outer diameter and 2 mm inner diameter where the coolant flows. All coils are connected electrically in series and appropriate electronic circuit (Fig. 3) allows

their independent switching. Such a configuration of magnetic fields produces a trap potential, harmonic near its minimum, with different frequencies in the axial and radial directions. The coils were planned to give the trap frequencies $\omega_a = 2\pi \times 12$ Hz and $\omega_r = 2\pi \times 137$ Hz at the current of 40 A and, indeed, the measured values are close to expectations (Sect. 4.1).

Controlling of the magnetic fields has to be appropriately fast and stable which is not trivial given the high inductance of the magnetic trap coils. Standard current control of stabilized power supplies is too slow for such purposes, so it was necessary to design a system based on MOSFET elements which allowed changing currents in the magnetic trap coils to accomplish the sequences such as shown in Fig. 4.

The schematic of the electronic control circuit is shown in Fig. 3. Keys K1, K2, and K3 are MOSFETs which are controlled by analogue signals applied to their gates via optocouplers. Crucial for reaching fast switching-off times was to quench the circuit ringing by sets of regular and Zener diodes connected parallel to the three conical (C) and two offset Helmholtz (H) coils of our magnetic trap. This system, powered by a set of high-stability power supply (PS) (Delta Electronica, SM15-200D), allowed switching off currents up to 60 A within 0.5 ms.

2.6. Laser system

The experiment makes use of several laser beams used for atom trapping/cooling, repumping, optical pumping, transfer between the traps, and imaging which differ in frequency, intensity, and polarization. The optical setup is

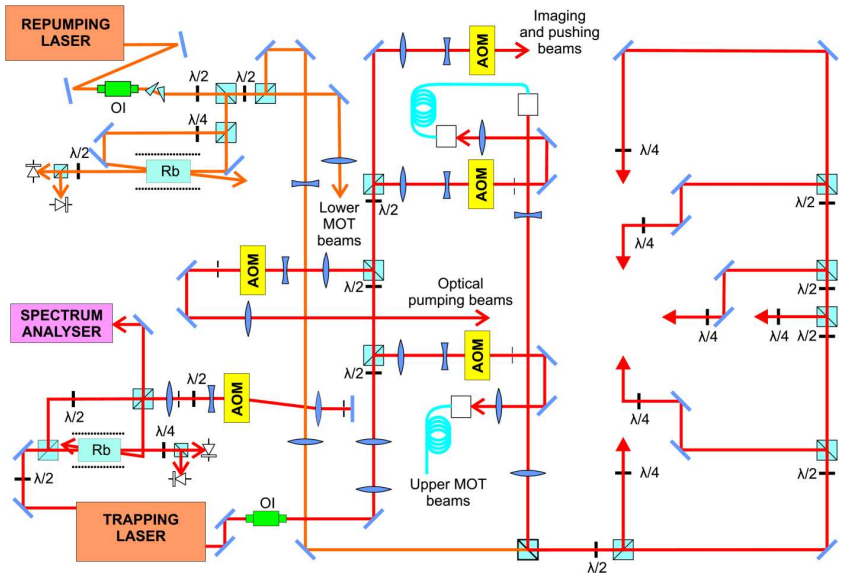

Fig. 5. Optical setup. OI indicates the optical isolator, AOM — acousto-optical modulator, Rb — the reference cells, $\lambda/2$ and $\lambda/4$ are the wave plates.

shown in Fig. 5. The beams are generated by two semiconductor lasers (Toptica, model TA100). Both lasers are stabilized to the atomic transition by the Doppler-free dichroism method [8]. One of the lasers produces the repumping light for both MOTs, tuned to the $F_{\mathrm{g}} = 1 - F_{\mathrm{e}} = 2$ transition. All other beams of frequencies close to the $F_{\mathrm{g}} = 2 - F_{\mathrm{e}} = 3$ resonant transition are produced by the other laser. Its output is split into individual beams by a series of polarization beam splitters, while the precise frequency tuning is achieved by the acousto-optical modulators (AOM). The transfer beam, trapping beam of the lower MOT, imaging beam, and the optical pumping beam are spatially filtered by sending them through short patch cords of single-mode, polarization-preserving optical fibers. This was important for reproducible atomic cloud shape in the lower MOT. The trapping and the repumping beams of the upper MOT were left unfiltered since this allowed to use more optical power while some distortions of the spatial beam profiles could be tolerated.

3. Experiment

3.1. Production of the condensate

The experiment begins with collecting atoms in the upper MOT (see the timing diagram in Fig. 4). Simultaneously, loading of the lower MOT by the transfer beam is started. The lower MOT loading lasts for 20 s and produces about 1×10^9 atoms of 500 μK in a cloud of maximum density 1×10^{11} cm^{-3}. The trapped atoms are further cooled in "cold MOT" for 3 ms. The cold MOT conditions are realized by increasing the trapping beams detuning from 2Γ to 6Γ. For the next 12 ms the atoms are kept in the optical molasses stage with the trapping beams at 6Γ detuning, but with no magnetic field. In this phase the atoms are not truly trapped but their escape is negligible since the temperature is only about 10 μK. Finally, the trapping and repumping beams are switched off and the atoms are transferred to the state in which they are magnetically trapped. Since in our setup we decide to trap magnetically atoms in the low-field-seeking $|F = 2, m_F = 2\rangle$ state, the trapping beams are switched off 500 μs before the repumping ones. Such a sequence optically pumps atoms into the $|F = 2\rangle$ state (hyperfine splitting (hfs) pumping), leaving them with almost equally populated Zeeman sublevels. In order to reach the final $|F = 2, m_F = 2\rangle$ state, the Zeeman pumping cycle is carried out. It consists in illuminating atoms by two short pulses of σ^+ polarized light, resonant with the $F_{\mathrm{g}} = 2 - F_{\mathrm{e}} = 2$ and $F_{\mathrm{g}} = 1 - F_{\mathrm{e}} = 2$ transitions, in presence of a weak homogeneous bias magnetic field of 1 G directed along z axis.

In this pumping scheme the final $|F = 2, m_F = 2\rangle$ state is the dark state, thus this process does not heat the atoms as it would be in the case of a closed (cycling) transition. The Zeeman pumping lasts for 2 ms at the pumping beam power of 3.4 mW/cm^2.

In the next step the magnetic trap is activated and its depth is gently increased. It is important to match the trap potential shape to the atomic cloud

shape, otherwise heating of atoms would cause losses. MT is therefore switched on at the low current when the potential well is shallow. For low potential depth the influence of the gravitational field is important: it shifts the overall potential minimum from the position of the magnetic field minimum and from the cloud center of mass. This gravitational sag is 3 mm in our case. To match the position of the cloud center with the trap center, an additional inhomogeneous magnetic field is applied in the vertical direction, which shifts the MOT trap after its loading and before the molasses phase. Such a solution assures efficient loading, properly running molasses phase and matches the cloud center to the potential minimum. Adjusting of the center and mode matching are crucial to avoid the cloud oscillations which cause atom heating.

In the next step, lasting for 2 s, the trap magnetic field is increased to the maximum value and the cloud is adiabatically compressed by switching on the offset coils. During this phase the cloud density increases at a cost of temperature in such a way that the phase density remains unchanged. After the compression and before further cooling the cloud is characterized by temperature $T = 100$ μK, density $n = 1 \times 10^{12}$ cm^{-3}, and atom number $N = 1 \times 10^8$. The efficiency of transfer of atoms from the lower MOT to MT is typically 70%.

3.2. Evaporative cooling

The last stage of the cooling process is the radio-frequency (RF) induced evaporation of atoms which is done by removing the fastest atoms from MT. The energy of the expelled atoms is higher than the average energy of remaining cloud. This causes the decrease in the temperature and simultaneous increase in phase-space density which is necessary for phase transition into the Bose–Einstein condensate [4]. The evaporation of atoms is controlled by RF radiation $\omega_{\rm rf}$ which is adjusted to be in resonance with the Zeeman splitting of $|F = 2\rangle$ state of the most energetic atoms in the trap. These atoms undergo spin-flips from the state $|F = 2, m_F = 2\rangle$, through the state $|F = 2, m_F = 1\rangle$, and eventually reach the untrapped states $|F = 2, m_F = 0, -1, -2\rangle$ so they are removed from the trap. Only the atoms with energy $E > \hbar|m_F|(\omega_{\rm rf} - \omega_0)$ can undergo this kind of radio-frequency induced spin-flips, where ω_0 denotes the RF frequency which corresponds to the bottom energy of MT. Crucial for efficient cooling is sufficiently high elastic collision rate. This rate was increased before evaporative cooling by adiabatic compression of the cloud caused by application of the offset field (coils H in Fig. 3).

The RF coil has two windings at a distance of 1.5 cm from the trap center. Symmetrically on the other side of the cell, an identical coil is terminated with 50 Ω. This yields homogeneous RF field distribution and better impedance matching. The power of RF radiation and the shape of its ramp are the adjustable parameters which can be used for improving the efficiency of the evaporation process [9]. We use nearly exponential ramp with RF frequency $\omega_{\rm rf}$ decreasing from 18 MHz to about 0.7 MHz within about 60 s (Fig. 6) and with the RF power of

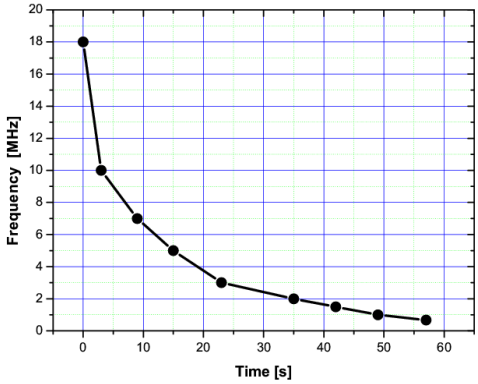

Fig. 6. Evaporative cooling. Exponential ramp with RF frequency ω_{rf} decreasing from 18 MHz to about 0.7 MHz with a time of ramping equal to 57 s.

6.4 W. The final result of evaporation cooling is transition to the Bose–Einstein condensate state.

3.3. Imaging

The imaging of the atomic cloud is done with a 150 μs pulse of circularly polarized laser light tuned to the $F_{\mathrm{g}} = 2, m_F = 2 - F_{\mathrm{e}} = 3, m_F = 3$ transition. The pulse can be triggered either *in situ*, when atoms are still in MT, or with some (2–30 ms) delay after their release from the trap. The beam is filtered by a single-mode optical fiber and expanded by a telescope to 1.7 cm diameter. A diaphragm selects the central beam part of 4 mm diameter with almost homogeneous intensity. This beam illuminates the condensate perpendicular to its axis. The absorption profile of the cloud is imagined on the CCD camera (Apogee, Alta USB) with a two-lens system. The first lens had focal length $f_1 = 125$ mm and the second was either $f_2 = 100$ mm or$f_2 = 250$ mm, which gave magnification of 0.87 or 2.11, respectively. The images yield information on the atomic density distribution in the cloud and allow derivation of other characteristics like the atom number and temperature.

4. Measurements of condensate dynamics

4.1. Determination of eigenfrequencies of the magnetic trap

Eigenfrequencies of atoms in the magnetic trap affect many parameters of the condensate and are the most essential characteristics of every experimental setup. There are two methods of measuring these frequencies. One is based on recording free oscillations of the atomic cloud induced by small perturbation, e.g. a shift of the trapping potential [10], the second method exploits parametric resonance of a thermal cloud in MT and the resulting atom number losses [11]. In the present work we use the first method. The MT control circuit, described in Sect. 2.5, allows for rapid current changes either in all trap coils, only in the conical coils, or only in the offset coils. Changing the current in all coils leads to a small shift of the MT center. This shift appears to be a convenient tool for inducing atom cloud

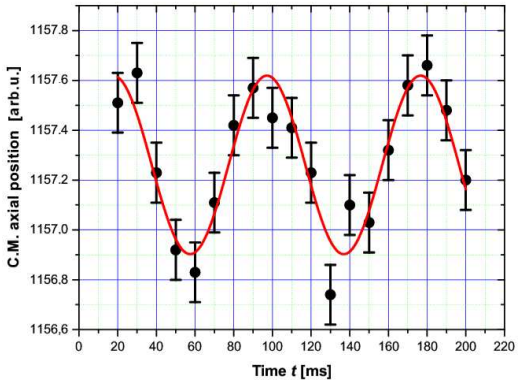

Fig. 7. Center of mass oscillations in a free fall in the axial direction.

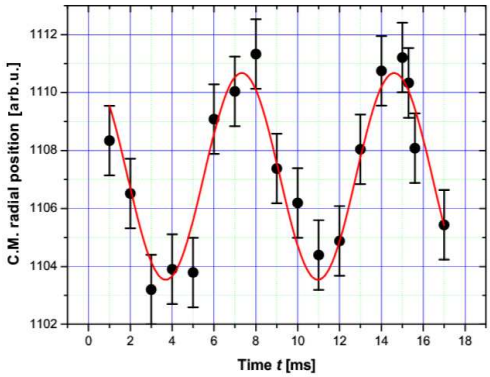

Fig. 8. Center of mass oscillations in a free fall in the radial direction.

oscillations. Changing the current for about 30 ms in all coils induces both dipolar and quadrupole cloud oscillations, whereas changes of the offset coil current result in radial dipole and in quadrupole oscillations. In this subsection we concentrate on the dipolar oscillations and discuss the quadrupole ones in the next subsection. Since the total current changes in all coils are relatively slow, only the slower axial dipole oscillations could be studied that way. On the other hand, the offset coil current could be altered sufficiently fast to allow study of the radial dipole oscillations. The perturbing current step was sufficiently low that the amplitude of the oscillations remained smaller than the condensate size. After the perturbation, the condensate oscillated in MT for time t, then was abruptly released from the trap and the image was taken after 20 ms of a free fall. Taking number of images for different t we observed oscillations of the center of mass in a free fall, the frequencies of which are equal to the trap frequencies [12] (Figs. 7 and 8). Sine function fit to the experimental data yielded the axial, $\omega_{\mathrm{a}} = 2\pi \times (12.6 \pm 0.3)$ Hz, and the radial, $\omega_{\mathrm{r}} = 2\pi \times (137 \pm 3)$ Hz, trap frequencies.

4.2. Fundamental quadrupole oscillation mode of the BEC

In addition to the center of mass shift, which is used to stimulate radial dipolar oscilations, change of the offset coil current affects also the trap shape and induces quadrupole oscillations of the BEC [12]. These oscillations can be conveniently analyzed by time-dependent Gross–Pitaevskii (GP) equation which for condensate of N atoms in a trapping potential $U(t)$ takes the form

$$\left[-\frac{\hbar^2}{2m}\nabla^2 + U(\boldsymbol{r},t) + Ng|\psi(\boldsymbol{r},t)|^2\right]\psi(\boldsymbol{r},t) = \mu\psi(\boldsymbol{r},t), \tag{1}$$

where m is the atomic mass, $g = 4\pi\hbar^2 a/m$ with a being the s-scattering length, μ is the chemical potential, and $\Psi(r,t)$ is the normalized wave function of the condensate. The term $Ng|\Psi(r,t)^2|$ represents the mean-field energy. In the so-called Thomas–Fermi (TF) regime the term associated with the kinetic energy is much weaker than the mean-field energy and can be neglected [13] which greatly simplifies the GP equation and yields analytical solution $\Psi(r)$:

$$\psi_{\mathrm{TF}}(\boldsymbol{r},t) = \sqrt{\frac{\mu - U(\boldsymbol{r},t)}{Ng}} \tag{2}$$

for $\mu \geq U(r,t)$ and $\Psi(r,t) = 0$, otherwise. The chemical potential is given by normalization

$$\mu = \frac{1}{2}\hbar\bar{\omega}\left(15Na\sqrt{\frac{m\bar{\omega}}{\hbar}}\right)^{2/5}, \tag{3}$$

where $\bar{\omega} = (\omega_x(0)\omega_y(0)\omega_z(0))^{1/3} = (\omega_{\mathrm{a}}\omega_{\mathrm{r}}\omega_{\mathrm{r}})^{1/3}$. The conditions of the Thomas-Fermi regime are well fulfilled when $Na/a_{\mathrm{HO}} \gg 1$, where $a_{\mathrm{HO}} = (\hbar/\omega_0 m)^{1/2}$ stands for the length of a harmonic oscillator of frequency ω_0. For ^{87}Rb atoms in the $5\ ^2S_{1/2}$, $|F = 2, m_F = 2\rangle$ state the scattering length $a \approx 5.3$ nm [14]. This means that for the measured oscillation frequencies of our trap the TF regime is fulfilled with $N \gg 260$. With this assumption the fundamental collective oscillation modes of a spherical symmetric trap of the ω_0 frequency can be described by the dispersion relation [15]:

$$\omega = \omega_0\sqrt{2n^2 + 2nl + 3n + l}, \tag{4}$$

where n is the radial mode number and l is the angular momentum. In the case of axially symmetric trap, the dispersion relation depends on m_l, i.e. projection of l on the trap axis. In special cases analytical solutions are possible. For example, for $m_l = \pm l$ and $m_l = \pm(l-1)$ one gets

$$\omega^2(m_l = \pm l) = l\omega_{\mathrm{r}}^2 \tag{5}$$

and

$$\omega^2[m_l = \pm(l-1)] = (l-1)\omega_{\mathrm{r}}^2 + \omega_{\mathrm{a}}^2. \tag{6}$$

The above equations fully describe the dipole excitation ($l = 1$), the frequencies of which agree with unperturbed harmonic oscillator frequencies. For the quadrupole modes ($l = 2$), solutions are available only for $m_l = \pm 2$ and $m_l = \pm 1$.

For $m_l = 0$ the solution is given by the dispersion relation

$$\omega^2(m=0) = \omega_{\rm r}^2 \left(2 + \frac{3}{2}\varepsilon^2 \mp \frac{1}{2}\sqrt{9\varepsilon^4 - 16\varepsilon^2 + 16}\right), \tag{7}$$

with $\varepsilon = \omega_{\rm a}/\omega_{\rm r}$. For the cigar geometry, $\varepsilon \ll 1$, which is the case of our experiment, the two oscillation frequencies are $\sqrt{5/2}\omega_{\rm a}$ and $2\omega_{\rm r}$. Changes of the offset coils current modify the radial trap extension, so only the fundamental quadrupole oscillation with $m_l = 0$ is excited. Like in the case of measurement of the trap eigenfrequencies a brief, 30 ms long, pulse was applied to the condensate. After time t of free oscillations the condensate was released from the trap and after 20 ms expansion in the free fall was imaged on the CCD camera.

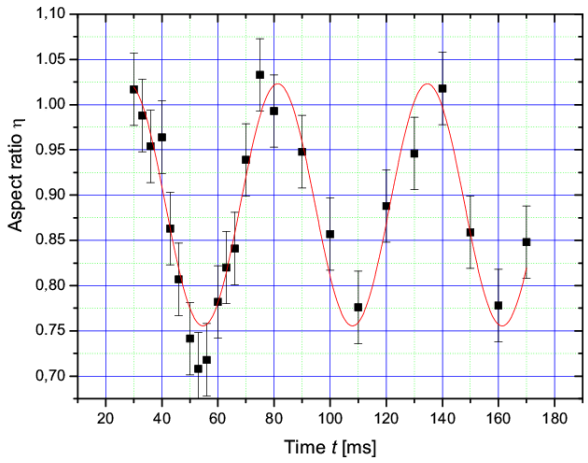

Fig. 9. Slow quadrupole oscillation mode. Sine function fitted to the aspect-ratio (η) dependence on t. (η is defined as the ratio of the radial and axial condensate TF radii).

The widths of the atomic cloud in axial and radial directions oscillated with approximately opposite phases. Since the imaging was performed after free expansion, the observed phase shift of these oscillations differed slightly from π. To reduce the effect of the atom-number fluctuations of the condensate on the measurements, the oscillation frequency was determined by sine function fitting to the aspect-ratio (η) dependence on t [16] (Fig. 9) (η is defined as the ratio of the radial and axial condensate TF radii). The measured value is $\omega_{\rm AR} = 2\pi \times (18.8 \pm 0.3)$ Hz which is to be compared with frequency $\sqrt{5/2}\omega_{\rm a} = 2\pi \times 19.9$ Hz. For our trap $\varepsilon \approx 0.09$ which does not fully comply with the assumption $\varepsilon \ll 1$ and results in small discrepancy between the measured and calculated values.

4.3. Free fall of BEC

In its free fall, the expanding condensate released from the trap remains in the TF regime [11], well described by the hydrodynamic equations [16] as being dependent on three time-dependent scaling parameters $\lambda_1, \lambda_2, \lambda_3$ with initial condition $\lambda_1 = \lambda_2 = \lambda_3 = 1$. For the cylindrically symmetric condensate, the aspect

ratio after releasing from the trap is given by

$$\eta(t) = \frac{W_{\mathrm{r}}(t)}{W_{\mathrm{a}}(t)} = \frac{\lambda_{\mathrm{r}}(t)}{\lambda_{\mathrm{a}}(t)}, \tag{8}$$

where W_{r} and W_{a} are the radial and axial condensate widths, respectively. The aspect ratio depends only on two parameters $\lambda_{\mathrm{r}} = \lambda_1 = \lambda_2$ and $\lambda_{\mathrm{a}} = \lambda_3$ and on the ratio of trap eigenfrequencies ε. These parameters evolve according to

$$\frac{\mathrm{d}^2}{\mathrm{d}\tau^2}\lambda_{\mathrm{r}} = \frac{1}{\lambda_{\mathrm{r}}^3\lambda_{\mathrm{a}}} \quad \text{and} \quad \frac{\mathrm{d}^2}{\mathrm{d}\tau^2}\lambda_{\mathrm{a}} = \frac{\varepsilon^2}{\lambda_{\mathrm{r}}^2\lambda_{\mathrm{a}}^2}, \tag{9}$$

where $\tau = \omega_r t$ is the dimensionless time. Equations (8) can be solved analytically for $\varepsilon \ll 1$. In the lowest order one gets

$$\lambda_{\mathrm{r}}(\tau) = \sqrt{1+\tau^2}, \tag{10}$$

$$\lambda_{\mathrm{a}}(\tau) = 1 + \varepsilon^2\left(\tau \arctan\tau - \ln\sqrt{1+\tau^2}\right). \tag{11}$$

As seen, λ_{r} grows much faster than λ_{a}, hence, after time of the order of $\tau \approx 1/\varepsilon$, the condensate changes its shape from the elongated (cigar-like) to the flattened one (pancake). In the TF regime the aspect ratio does not depend on atom number N.

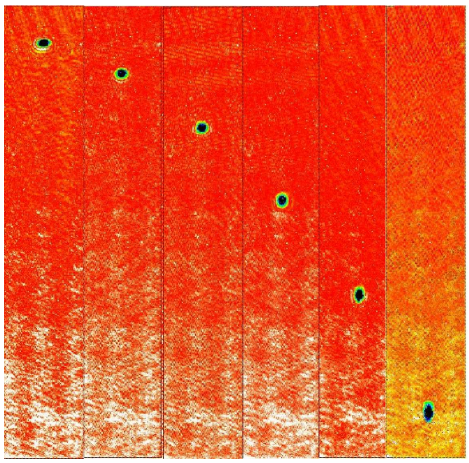

Fig. 10. Condensate images taken for different free fall times in 5 ms intervals.

Figure 10 collects condensate images taken for different free fall times in 5 ms time intervals. The corresponding aspect ratios are shown in Fig. 11 along with the theoretical prediction of solutions (10) and (11) (solid line) and with the expansion of an ideal thermal gas cloud (broken line). The experimental dependence clearly indicates that the released atoms exhibit behavior consistent with the Thomas–Fermi model of a quantum, superfluid gas.

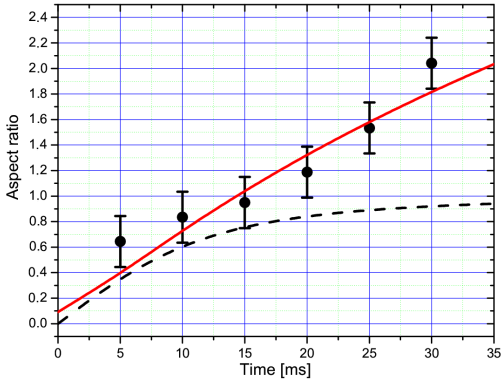

Fig. 11. Aspect ratio of BEC during free fall along with the theoretical prediction of solutions (10) and (11) (solid line) and with the expansion of an ideal thermal gas cloud (broken line).

5. Summary and outlook

The described study yields basic hydrodynamic properties of our condensate. Qualitatively, they are consistent with observations of other authors for similar systems [17, 18], nevertheless, as each BEC setups are different, such properties need to be determined for each specific system. We have measured fundamental frequencies of the MT which determine dynamics of the condensate in our apparatus. Measurements of the free fall evolution revealed basic hydrodynamic properties of the trapped atom sample which are consistent with the Thomas–Fermi model. They provide clear evidence of the quantum, superfluid character of the atom cloud and form the sound basis for interpretation of future experiments with the condensate.

Acknowledgments

The authors benefited from numerous discussions with many colleagues from LENS (Florence), ENS (Paris), Amsterdam, Berkeley, Hannover, Innsbruck, Munich, Pisa, and Stuttgart. We wish to express our particular thanks to Jean Dalibard, Chiara Fort, and Giacomo Roati for their patient and most valuable advices and Massimo Inguscio for continuous encouragement.

This work was supported by the research grants of the Polish Ministry of Science 1PO3B 017 29 and PBZ/KBN/043/PO3/2001.

References

[1] J. Söding, D. Guéry-Odelin, P. Desbiolles, F. Chevy, H. Inamori, J. Dalibard, *Appl. Phys. B.* **69**, 257 (1999).

[2] M.H. Anderson, J.R. Ensher, M.R. Matthews, C.E. Wieman, E.A. Cornell, *Science* **269**, 198 (1995).

[3] K.B. Davis, M.-O. Mewes, M.R. Andrews, N.J. van Druten, D.S. Durfee, D.M. Kurn, W. Ketterle, *Phys. Rev. Lett.* **75**, 3969 (1995).

[4] W. Ketterle, D.S. Durfee, D.M. Stamper-Kurn, cond-mat/9904034, 1999, in: *Proc. Int. School of Physics Enrico Fermi,* Course CXL, M. Inguscio, S. Stringari, C.E. Wieman, IOS Press, Amsterdam, 1999 p. 67.

[5] U.D. Rapol, A. Wasan, V. Natarajan, *Phys. Rev. A* **64**, 023402 (2001).

[6] E. Majorana, *Nuovo Cimento* **9**, 43 (1932).

[7] T. Esslinger, I. Bloch, T.W. Hänsch, *Phys. Rev. A* **58**, R2664 (1998).

[8] G. Wąsik, W. Gawlik, J. Zachorowski, W. Zawadzki, *Appl. Phys. B* **75**, 1 (2002).

[9] J.E. Lye, C.S. Fletcher, U. Kallmann, H.-A. Bachor, J.D. Close, *J. Opt. B: Quantum Semiclass. Opt.* **4**, 57 (2002).

[10] M.-O. Mewes, M.R. Andrews, N.J. van Druten, D.M. Kurn, D.S. Durfee, C.G. Townsend, W. Ketterle, *Phys. Rev. Lett.* **77**, 988 (1996).

[11] U. Ernst, J. Schuster, F. Schreck, A. Martel, A. Kuhn, G. Rempe, *Appl. Phys. B* **67**, 719 (1998).

[12] D.S. Jin, J.R. Ensher, M.R. Matthews, C. E. Wieman, E.A. Cornell, *Phys. Rev. Lett.* **77**, 420 (1996).

[13] G. Baym, C.J. Pethick, *Phys. Rev. Lett.* **76**, 6 (1996).

[14] J.R. Gardner, R.A. Cline, J.D. Miller, D.J. Heinzen, H.M.J.M. Boesten, B.J. Verhaar, *Phys. Rev. Lett.* **74**, 3764 (1995).

[15] S. Stringari, *Phys. Rev. Lett.* **77**, 2360 (1996).

[16] Y. Castin, R. Dum, *Phys. Rev. Lett.* **77**, 5315 (1996).

[17] D.S. Jin, M.R. Matthews, J.R. Ensher, C. E. Wieman, E.A. Cornell, *Phys. Rev. Lett.* **78**, 764 (1997).

[18] D.M. Stamper-Kurn, H.-J. Miesner, S. Inouye, M.R. Andrews, W. Ketterle, *Phys. Rev. Lett.* **81**, 500 (1998).